

PAPER

Three-dimensional porous $\text{Co}_3\text{O}_4\text{-CoO@GO}$ composite combined with N-doped carbon for superior lithium storage

To cite this article: Yanan Xu *et al* 2019 *Nanotechnology* **30** 425404

View the [article online](#) for updates and enhancements.





IOP | ebooksTM

Bringing you innovative digital publishing with leading voices to create your essential collection of books in STEM research.

Start exploring the collection - download the first chapter of every title for free.

Three-dimensional porous $\text{Co}_3\text{O}_4\text{-CoO@GO}$ composite combined with N-doped carbon for superior lithium storage

Yanan Xu¹, Cong Wu¹, Liyuan Ao¹, Kai Jiang¹, Liyan Shang¹, Yawei Li¹ ,
Zhigao Hu^{1,2,3}  and Junhao Chu^{1,2,3}

¹ Technical Center for Multifunctional Magneto-Optical Spectroscopy (Shanghai), Department of Electronic Engineering, East China Normal University, Shanghai 200241, People's Republic of China

² Collaborative Innovation Center of Extreme Optics, Shanxi University, Taiyuan, Shanxi 030006, People's Republic of China

³ Shanghai Institute of Intelligent Electronics & Systems, Fudan University, Shanghai 200433, People's Republic of China

E-mail: zghu@ee.ecnu.edu.cn

Received 26 April 2019, revised 28 June 2019

Accepted for publication 9 July 2019

Published 6 August 2019



CrossMark

Abstract

Transition metal oxides (TMOs) as anode materials have potential for lithium-ion batteries (LIBs). However, the poor rate capacity and cycle stability restrict its application. Herein, we demonstrate a facile one-step hydrothermal method to construct a three-dimensional porous conductive network structure, which consists of thin-layered graphene, ultrafine $\text{Co}_3\text{O}_4\text{-CoO}$ nanoparticles and nitrogen-doped carbon. This unique structure can effectively prevent particle agglomeration and cracking caused by volume expansion, provide fast passage for lithium ion/electron transport during cycling and improve the electrical conductivity of the electrode. Moreover, the electrochemical kinetic analysis proves that this is a process dominated by pseudocapacitive behavior. Consequently, the N-C@ $\text{Co}_3\text{O}_4\text{-CoO@GO}$ hybrid electrode delivers an ultrahigh capacity of 1 273.1 mA h g^{-1} at 0.1 A g^{-1} and superior rate performance (725.1 mA h g^{-1} at 5 A g^{-1}). Additionally, it exhibits a high reversible cycling capacity of 787.4 mA h g^{-1} at 1 A g^{-1} over 600 cycles and even maintains excellent cycling stability for a ultra-long cycles at 5 A g^{-1} . This work provides a feasible strategy for fabricating the N-C@ $\text{Co}_3\text{O}_4\text{-CoO@GO}$ composite as a promising high-performance TMOs anode for LIBs.

Supplementary material for this article is available [online](#)

Keywords: transition metal oxides, three-dimensional porous structure, N-doped carbon, ultrahigh capacity, superior rate performance

(Some figures may appear in colour only in the online journal)

1. Introduction

In recent years, the increasing demand for energy has resulted in a sharp increase in the use of fossil fuels, which has led to the deterioration of the global environment and the emergence of extreme weather. It is particularly eager to develop sustainable and renewable energy sources. Hence, lithium-ion batteries (LIBs) have attracted great attention as green power energy source, which have been widely used in portable

electronic devices, energy vehicles and smart energy grids [1–3]. However, the most commonly used graphene anode material for LIBs has a relatively low theoretical specific capacity (only 372 mAh g^{-1}) and is difficult to satisfy the growing demand for energy storage devices [4]. Therefore, it is imperative to explore alternative anode materials with high specific capacity. Due to the high theoretical capacity, low cost, and abundant natural reserves, transition metal oxides (TMOs) have attracted much attention as the anode materials

for LIBs [5–12]. Among the promising TMO materials, Co_3O_4 has received great attention because of its high theoretical capacity (890 mA h g^{-1}). Moreover, the cobalt oxide-based materials have great potential applications in the full cell, which exhibits certain advantages compared with traditional graphene [13, 14]. Nonetheless, the intrinsic defects of TMOs, such as poor electrical conductivity and volume expansion during lithiation/delithiation process, lead to severe capacity degradation, poor rate performance and inferior cycle stability [15, 16]. Therefore, it is a great challenge to solve the above problem of TMOs for LIBs.

Great efforts have been made to alleviate the inherent defects. One effective method involves the synthesis of nanostructures such as nanocubes [17], nanosheets [18–20], nanoparticles [21, 22], nanowires [23, 24], nanospheres [25] and so on. The nano-sized materials provide more active sites for electrochemical reactions, shorten the Li^+ diffusion length and accommodate the volume changes during the insertion/extraction processes. What is more, the construction of porous/hollow structures can accelerate the transport of lithium ions and improve the electrochemical performance of the anode materials [26, 27]. Combining the transition metal oxide with carbonaceous material (e.g. carbon nanofiber [28], carbon nanotubes [29], graphene [30] and conducting polymers [31]) is the other feasible strategy. Graphene is an excellent carbon-based material that has attracted much attention due to its high electrical conductivity and superior flexibility. It not only enhances electron transport and ion diffusion but also moderates volume expansion, improving structural stability. In addition, nitrogen-doped carbon is an extremely attractive approach to improve electrical performance [32–34]. It was previously reported that the doping of nitrogen atoms can produce extrinsic defects, which lead to enhanced carbon reactivity and conductivity. Moreover, nitrogen doping can provide more active sites for lithium ion reactions and enhance carbon-lithium interactions, which significantly improve Li^+ reaction kinetics. Another accessible approach is to combine two different metal oxides for improving the rate and cycle performance with the aid of the synergetic effect between them. For example, the hybrids of Co/CoO nanoparticles [35], $\text{Co}_3\text{O}_4/\text{Fe}_2\text{O}_3$ composite [36], $\text{Co}_3\text{O}_4/\text{TiO}_2$ hybrids [37], $\text{SnO}_2/\text{Co}_3\text{O}_4$ [38] and $\text{Co}_3\text{O}_4/\text{ZnO}$ hybrids [39] exhibit higher reversible capacity compared to the single component. However, there is rarely the application of the $\text{Co}_3\text{O}_4/\text{CoO}$ compound as an anode electrode material for LIBs until now.

Herein, we introduce a simple one-step hydrothermal method to fabricate a three-dimension network structured N-C@ Co_3O_4 -CoO@GO hybrid. Owing to the distinctive architecture, the as-synthesized N-C@ Co_3O_4 -CoO@GO anode exhibits the following superior properties: (1) Porous structure of Co_3O_4 -CoO nanoparticles facilitate the penetration of electrolytes and enhances the diffusion of lithium ions. (2) The Co_3O_4 -CoO nanoparticles are homogeneously anchored between thin-layered graphene oxide, which relieve the volume expansion of the material during the cycling process. Besides, the flexible graphene not only improves electrical conductivity but also maintains structural stability.

(3) The addition of N-doped carbon source supply more active sites to further enhance conductive properties and reaction kinetics for the electrode. As a consequence, the N-C@ Co_3O_4 -CoO@GO composite reveals highly superior electrochemical performance under the stimulation of above virtues, suggesting that the N-C@ Co_3O_4 -CoO@GO electrode could be a promising candidate for next-generation LIB anodes.

2. Experimental section

2.1. Material preparation

Generally, graphene oxide (GO) was synthesized by a modified Hummers' method from natural graphite nanoflakes [40]. In a typical way, 100 mg graphite powder were dissolved in 20 ml deionized water (DI), stirred for 24 h at room temperature and then ultra-sonicated for 1 h. Next, 1.6 g $\text{Co}(\text{CH}_3\text{COO})_2 \cdot 4\text{H}_2\text{O}$ and 0.7 g NaOH were dissolved into 50 ml ethanol and stirred to form a homogeneous solution, followed by the addition of 0.5 g polyvinyl pyrrolidone (PVP). After that, the GO suspension was added gradually into the above mixture under continuous magnetic stirring. Finally, the mixed solution was transferred into a 100 ml Teflon-lined stainless autoclave, which was heated at 180°C for 12 h. When the autoclave was cooled naturally to room temperature, the obtained precipitate was washed with DI water and ethanol and dried at 80°C for 24 h. To obtain N-C@ Co_3O_4 -CoO@GO, the dried powder was heated at 350°C for 3 h under an argon atmosphere. For comparison, Co_3O_4 -CoO@GO and Co_3O_4 -CoO were synthesized by a similar method without PVP or GO. We also performed annealing treatment at 250 and 450°C to obtain the pure Co_3O_4 and CoO, respectively.

2.2. Materials characterization

The crystal structures of all samples were identified by x-ray diffraction (XRD, Bruker D8 diffractometer) analyses with Cu-K α radiation ($\lambda = 1.5418 \text{ \AA}$) at a scanning speed of 5° min^{-1} from 10° to 80° . X-ray photoelectron spectroscopy (XPS, RBD upgraded PHI-5000C ESCA system) was measured with Mg-K α radiation ($h\nu = 1253.6 \text{ eV}$). Raman spectra were obtained by a micro-Raman spectrometer (Jobin-Yvon LabRAM HR 800UV) with an excitation laser beam wavelength of 532 nm. The morphological features of samples were characterized by using scanning electron microscopy (SEM, JEOL-JSM-6700F) equipped with x-ray energy dispersive spectroscopy (EDS). Transmission electron microscopy (TEM, FEI Tecnai G20 TEM) and high-resolution TEM (HRTEM) were operated at a voltage of 200 kV. The Brunauer-Emmett-Teller (BET) surface areas and density functional theory (DFT) pore diameter distributions were investigated using a TriStar II 3020 instrument. Thermogravimetric analysis (TGA) was carried out with thermal analysis (TA) instruments.

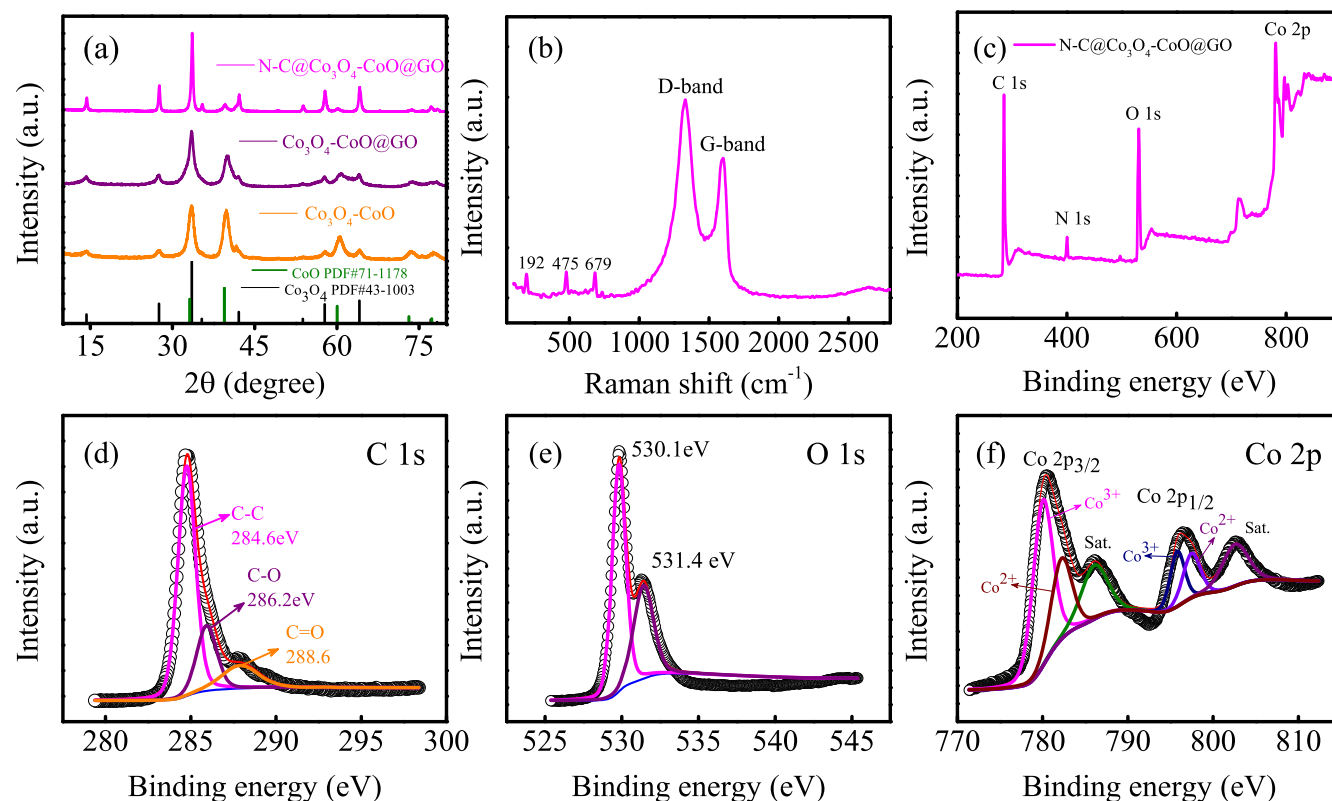


Figure 1. (a) XRD patterns of the as-synthesized N-C@Co₃O₄-CoO@GO, Co₃O₄-CoO@GO and Co₃O₄-CoO composites. (b) Raman spectra and (c) survey XPS spectrum of N-C@Co₃O₄-CoO@GO composite. High-resolution XPS spectrum of (d) C 1s, (e) O 1s and (f) Co 2p, respectively.

2.3. Electrochemical measurement

The working electrodes were fabricated by coating copper foil with a slurry composed of active material, acetylene black (as a conducting agent) and polyvinylidene fluoride (as a binder) at a weight ratio of 7:2:1 in an *n*-methyl-2-pyrrolidinone (NMP) solvent, followed by drying in a vacuum oven at 60 °C overnight. The loading mass of active materials on each working electrode with a diameter of 14 mm was about 0.8 mg cm⁻². For electrochemical measurement, the CR2025-type half-cells were assembled in a glove box under an argon-filled atmosphere. Lithium foil and a Celgard 2400 membrane were used as a counter electrode and separator, respectively. 1.0 M LiPF₆ solution dissolved in a mixture of ethylene carbonate, diethyl carbonate and ethyl methyl carbonate with a volume ratio of 1:1:1 was used as the electrolyte. Galvanostatic charge/discharge tests of the as-prepared batteries were conducted on a LAND CT 3001A system in a voltage range of 0.01–3.0 V (versus Li/Li⁺). The cyclic voltammetry (CV) and electrochemical impedance spectroscopy (EIS) were fulfilled on a CHI660 electrochemical workstation. The CV tests were performed at a sweep rate of 0.1–10 mV s⁻¹ within a potential range of 0.01–3 V. The EIS measurements were conducted by employing an alternating current (AC) voltage of 5 mV amplitude in a frequency range of 100 kHz–0.01 Hz.

3. Results and discussion

3.1. Structure and composition analysis

To investigate the effect of annealing temperature on the purity and crystalline phase, the samples were annealed at different temperatures. In figure S1, available online at stacks.iop.org/NANO/30/425404/mmedia, pure CoO (JCPDS# 71-1178) and Co₃O₄ (JCPDS# 43-1003) were formed at 250 and 450 °C, respectively. Then we obtained the mixed phase at intermediate temperatures. The XRD patterns of as-prepared N-C@Co₃O₄-CoO@GO composites and the comparisons are shown in figure 1(a). Obviously, the diffraction peaks with the 2θ values located at 19°, 31.2°, 36.8°, 38.5°, 44.8°, 55.6°, 59.3° and 65.2° can be indexed to the (111), (220), (311), (222), (400), (422), (511) and (440) crystal faces, which were in good agreement with the standard phase of Co₃O₄ (JCPDS# 43-1003) [41]. Besides, the peaks at 2θ angles of around 36.4°, 42.3°, 61.4°, 73.6° and 77.5° are consistent with the (111), (200), (220), (311) and (222) planes of CoO (JCPDS# 71-1178), respectively [42]. Moreover, it can be seen that there are no miscellaneous peaks in the XRD patterns, revealing the high purity and good crystallinity of the composite. In the Raman spectra of N-C@Co₃O₄-CoO@GO (figure 1(b)), three obvious peaks can be observed at ~192, 475 and 679 cm⁻¹ corresponding to vibration mode of Co₃O₄ and CoO, respectively [35, 43]. Besides, the spectra exhibits

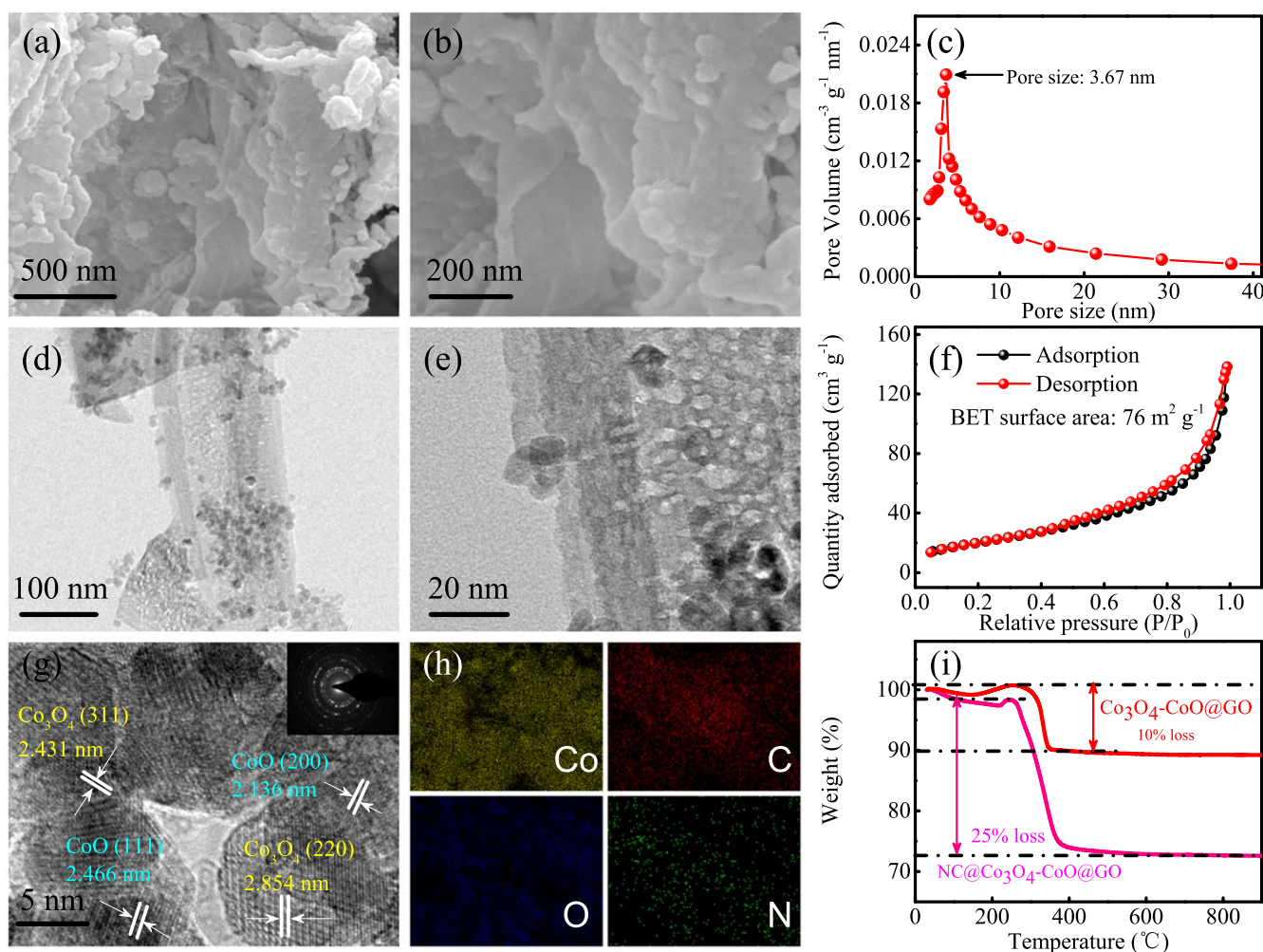


Figure 2. (a) SEM and (b) high-magnification SEM images of N-C@Co₃O₄-CoO@GO. (d) TEM and (e) HRTEM images of N-C@Co₃O₄-CoO@GO. (g) HRTEM image of N-C@Co₃O₄-CoO@GO. (h) Element mapping of N-C@Co₃O₄-CoO@GO composite for Co, C, O, N. (c) pore size distribution curve and (f) N₂ adsorption/desorption isotherms of N-C@Co₃O₄-CoO@GO. (i) TGA curves of N-C@Co₃O₄-CoO@GO and Co₃O₄-CoO@GO composites.

two characteristic peaks at $\sim 1331\text{ cm}^{-1}$ (the D band due to defective and disordered carbon) and 1596 cm^{-1} (the G band due to sp^2 hybridized and ordered graphitic carbon). The intensity of ratio for the D band to G band (I_D/I_G) is 1.41, which implies that the composite is a defective and disordered structure [44]. The XPS analysis is used to confirm the composition and chemical valence state of elements. Figure 1(c) shows the XPS spectrum of N-C@Co₃O₄-CoO@GO. We can observe four signal peaks at ~ 285 , 399, 531, and 780–803 eV, accurately corresponding to the C 1s, N 1s, O 1s and Co 2p, respectively. It indicates the existence of above elements in the composites. The high-resolution spectra of Co 2p (figure 1(f)) contains two spin-orbit peaks Co 2p_{3/2} (located at 780.5 eV) and Co 2p_{1/2} (located at 796.6 eV), which indicates Co³⁺ and Co²⁺ coexisting in N-C@Co₃O₄-CoO@GO. Additionally, two shake-up satellite peaks at 786.1 eV and 802.6 eV, demonstrate the presence of a Co²⁺ state in the complex [45, 46]. The XPS peaks appear in O 1s spectrum (figure 1(e)), where the peak of 530.1 eV is related to Co–O band and the peak of 531.4 eV corresponds to defect of oxygen vacancy and surface adsorption of oxygen species [47]. The high resolution

C 1s spectrum (figure 1(d)) can be divided into three peaks, located at 284.6 eV (C–C), 286.2 eV (C–O/C–N), 288.6 eV (C=O) [33, 35]. The XPS spectra of N 1s contains three main peaks around 398.7, 399.9 and 400.6 eV, corresponding to pyridinic, pyrrolic and graphitic N, respectively (figure S2) [28, 33]. Notably, nitrogen doping can be beneficial in helping to improve the conductivity of carbon-based materials and electrical properties of composites.

3.2. Surface morphologies

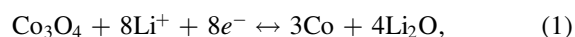
In order to explore the morphology and microstructure of the synthesized materials, we performed SEM and TEM characterization of N-C@Co₃O₄-CoO@GO, Co₃O₄-CoO@GO and Co₃O₄-CoO. From the SEM images (figures 2(a), (b)), we can observe that the graphene flakes interweave with each other, self-assembling to form a three-dimensional framework. Such architecture not only provides numerous sites for the nucleation growing of nanoparticles but also prevents nanoparticle agglomeration. On the surface of the graphene flakes, the nanoparticles of Co₃O₄ and CoO are uniformly

dispersed. What is more, these dispersed nanoparticles can effectively prevent graphene sheet agglomeration. Besides, these small particles can also contribute to the insertion and extraction of lithium ions during the electrochemical reaction. The morphology of $\text{Co}_3\text{O}_4\text{-CoO@GO}$ and $\text{Co}_3\text{O}_4\text{-CoO}$ are shown in figure S3. The SEM image of $\text{Co}_3\text{O}_4\text{-CoO@GO}$ is similar to that of $\text{N-C@Co}_3\text{O}_4\text{-CoO@GO}$. It suggests that the introduction of N-doped carbon cannot destroy the structural integrity but enhance the electrical conductivity. Evidently, the nanoparticles of $\text{Co}_3\text{O}_4\text{-CoO}$ are agglomerated together, indicating the important role of the graphene sheets and N-doped carbon in the structure and properties of the composites. Moreover, the TEM images of $\text{N-C@Co}_3\text{O}_4\text{-CoO@GO}$ (figures 2(d), (e)) reveal a three-dimensional integrated interconnected network. It is clear that the graphene sheets are very transparent, indicating that they are single or few layers. Graphene sheets are connected with each other and compose a stable structure. Compared with $\text{Co}_3\text{O}_4\text{-CoO}$ (figures S4(c), (d)), the TEM images of $\text{N-C@Co}_3\text{O}_4\text{-CoO@GO}$ and $\text{Co}_3\text{O}_4\text{-CoO@GO}$ (figures S4(a), (b)) further confirm that the nanoparticles are homogeneously distributed on the graphene substrate, consistent with the result of the SEM images. Such a structure would be favorable for the effective penetration of electrolytes and rapid diffusion of lithium ions. At the same time, this multidimensional structure is equivalent to an electronic transmission highway. Furthermore, it can effectively relieve the stress effects caused by volume expansion. The HRTEM image (figure 2(g)) exhibits distinct lattice fringes with a spacing distance of 2.431 and 2.854 nm, corresponding to the (311) and (220) crystal planes of Co_3O_4 . Meanwhile, the lattice spacing of 2.136 and 2.466 nm can be indexed to the (200) and (111) crystal planes of CoO . This HRTEM image confirms that the as-prepared compounds consist of the Co_3O_4 and CoO phases, which is consistent with the XRD results. The selected area electron diffraction (SAED) pattern in the inset of figure 2(g) shows a series of concentric rings, suggesting the polycrystalline nature of the products. The spatial distribution of different elements in the $\text{N-C@Co}_3\text{O}_4\text{-CoO@GO}$ composite was investigated by elemental mapping analysis. In figure 2(h), the mapping images show a uniform element distribution of Co, O, C and N elements, matching well with the analysis of XPS. For further analysis of the surface structure and porosity of the material, we performed Barret–Joyner–Halenda (BJH) pore size distribution and BET measurements. From figure 2(c), we can conclude that the pore size of the sample is mostly around 3.67 nm, implying the mesoporous properties of the $\text{N-C@Co}_3\text{O}_4\text{-CoO@GO}$ nanocomposite. In addition, the high specific surface area is about $76 \text{ m}^2 \text{ g}^{-1}$, which facilitates the electrolyte penetration to realize more sufficient contact between the active material and electrolyte (figure 2(f)). Moreover, it realizes faster electrons transfer to improve electrochemical performance. To further analyze the carbon content of the materials, we performed TGA analysis. As shown in figure 2(i), there is a distinguishable weight loss existing at about 400°C , which is ascribed to the combustion of carbonaceous materials and the conversion into gaseous substances. Specifically, the loss of carbon content of the $\text{N-C@Co}_3\text{O}_4\text{-CoO@GO}$ (25%) and $\text{Co}_3\text{O}_4\text{-CoO@GO}$ (10%) can further show the successful

incorporation of the nitrogen-containing carbon component. Particularly, a slight weight increasing phenomenon appears at $\sim 250^\circ\text{C}$, which may be due to oxidation of CoO which completely transformed into Co_3O_4 . We also performed XRD characterization of $\text{N-C@Co}_3\text{O}_4\text{-CoO@GO}$ and $\text{Co}_3\text{O}_4\text{-CoO@GO}$ after 500°C annealing in air atmosphere. In figure S5, all the XRD characteristic peaks of both samples match with the phase Co_3O_4 (JCPDS# 43-1003), which confirms the above conclusion well.

3.3. Energy storage applications

The electrochemical performance of LIBs made from $\text{N-C@Co}_3\text{O}_4\text{-CoO@GO}$ as the anode material was evaluated by a CV experiment. Figure 3(a) shows the first five CV curves of the $\text{N-C@Co}_3\text{O}_4\text{-CoO@GO}$ at a scanning rate of 0.5 mV s^{-1} from 0.01 to 3.0 V. Two peaks appear at $\sim 0.80 \text{ V}$ and $\sim 1.24 \text{ V}$ in the first cycle of cathodic scan, which is caused by the reduction of Co_3O_4 and CoO to metal Co , accompanied by the formation of Li_2O and solid electrolyte interface (SEI) layers. Additionally, a slight shift happens to these peaks in the subsequent cycles. It is due to irreversible formation of the SEI film and structural modification arises from Li^+ insertion/extraction [48, 49]. In the following oxidation scan, there are two anodic peaks located at $\sim 1.38 \text{ V}$ and $\sim 2.1 \text{ V}$. The one at $\sim 1.38 \text{ V}$ may be due to the extraction of Li^+ from carbon and the partial decomposition of SEI layers [35, 42]. While the other peak at $\sim 2.1 \text{ V}$ is attributed to the reversible oxidation of Co to Co_3O_4 and CoO , accompanied by the decomposition of Li_2O . All in all, the electrochemical reactions during the discharge/charge process can be described as follows [50–53]:



Apart from the first cathodic scan, the following cathodic scanning curves are almost overlapping, indicating good cycling stability and reversible electrochemical reaction. The galvanostatic discharge and charge curves of five cycles for $\text{N-C@Co}_3\text{O}_4\text{-CoO@GO}$ at a current density of 0.1 A g^{-1} from 0.01 to 3 V is observed in figure 3(b). The first discharge and charge specific capacity are 1138.9 and $800.8 \text{ mA h g}^{-1}$, respectively. Therefore, the resulting initial coulombic efficiency (CE) is 70.3% and the irreversible capacity loss may be caused by the formation of the SEI film during decomposition of the electrolyte. Besides, attributing to the gradual activation of the electrode and the formation of active sites during the insertion and extraction of Li^+ ions, the specific capacity of charge and discharge increases to some extent, thus the ratio of charge and discharge specific capacity (CE) gradually increases and tends to a stable value compared with the first cycle [54–56]. The approximate CE in the subsequent cycle demonstrates the excellent stable and reversible cycle performance in accord with CV analysis.

The comparison of rate performance from $\text{N-C@Co}_3\text{O}_4\text{-CoO@GO}$, $\text{Co}_3\text{O}_4\text{-CoO@GO}$, $\text{Co}_3\text{O}_4\text{-CoO}$ at different current densities (0.1 A g^{-1} – 5 A g^{-1}) are shown in figure 3(c). The sample of $\text{N-C@Co}_3\text{O}_4\text{-CoO@GO}$ achieves reversible

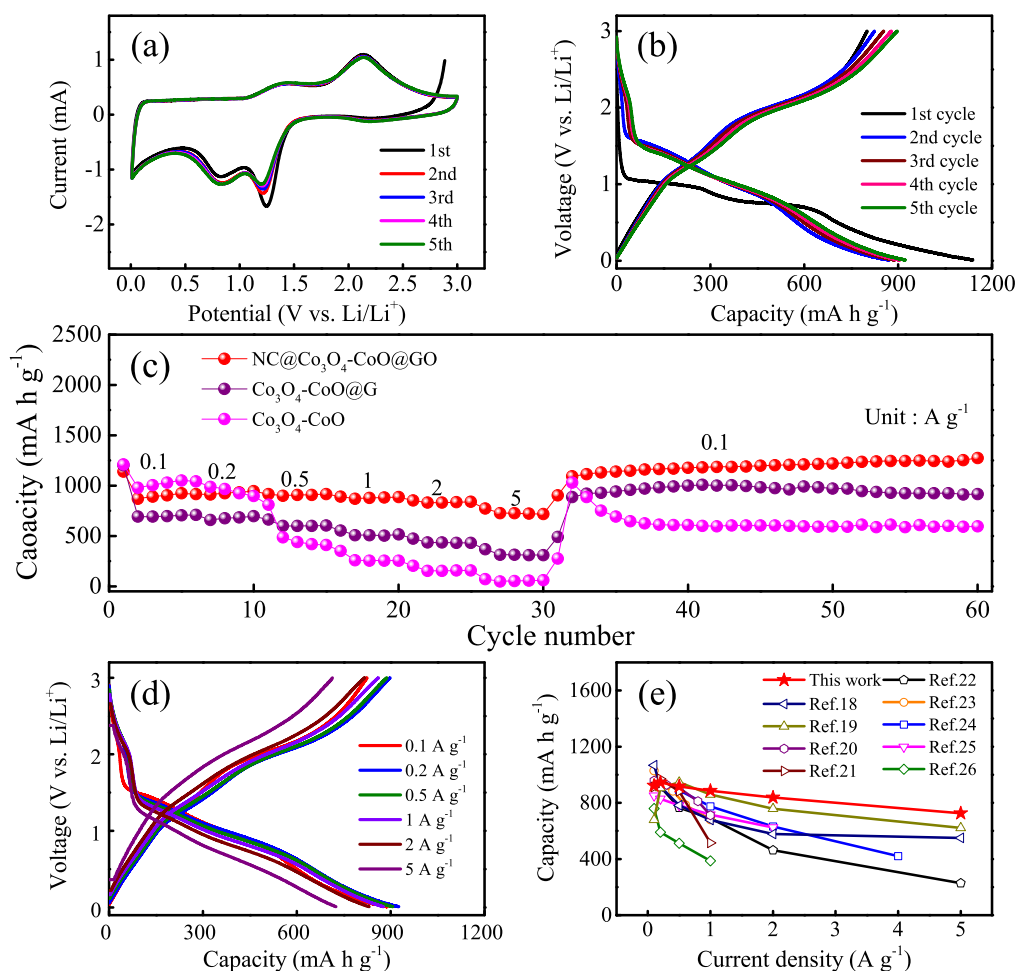


Figure 3. (a) CV curves of the N-C@Co₃O₄-CoO@GO composite at a scan rate of 0.5 mV s⁻¹ within the range of 0.01–3.0 V. (b) Galvanostatic charge/discharge curves of N-C@Co₃O₄-CoO@GO composite at a current density of 0.1 A g⁻¹. (c) Comparison of the rate capacity of N-C@Co₃O₄-CoO@GO, Co₃O₄-CoO@GO and Co₃O₄-CoO at various current densities ranging from 0.1 to 5.0 A g⁻¹. (d) Charge/discharge curves of N-C@Co₃O₄-CoO@GO at different current densities (0.1 ~ 5.0 A g⁻¹). (e) The comparison of the rate performance of materials in this work and previous Co₃O₄-based work in the literature.

specific capacities of 922.7, 944.9, 916.9, 885.9, 838.8 and 725.1 mA h g⁻¹ at the current densities of 0.1, 0.2, 0.5, 1, 2 and 5 A g⁻¹, respectively. When the current density returns to 0.1 A g⁻¹, the discharge capacity can recover to 1092.7 mA h g⁻¹ and remain stable after 30 cycles, which still reaches and exceeds the initial capacity. The N-C@Co₃O₄-CoO@GO exhibits the best rate capability among all the samples, indicating excellent structural stability. Figure 3(d) and figure S6 present the corresponding charge and discharge curves of the rate performance from figure 3(c). Compared to Co₃O₄-CoO@GO and Co₃O₄-CoO, N-C@Co₃O₄-CoO@GO exhibits a higher and more stable specific capacity, which is consistent with the results of figure 3(c). Moreover, the cycle performance of N-C@Co₃O₄-CoO@GO, Co₃O₄-CoO@GO and Co₃O₄-CoO measured at 1.0 A g⁻¹ with the first five-cycle activation process at 0.1 A g⁻¹ are displayed in figure 4(c). When it refers to N-C@Co₃O₄-CoO@GO, there is an obvious fluctuation appearing during the cycling process, which is a common phenomenon in the previous reports on TMOs for LIBs [43, 57]. The gradual rise at the beginning of the cycling is mainly due to the gradual formation of an SEI film and the

activation process caused by the transition of the crystalline phase to amorphous structure of the active material, which accelerates the diffusion of lithium ions [58, 59]. In the subsequent cycles, the specific capacity decreases slightly and maintains stability due to the stabilization of the SEI film and the completion of the activation process. At the 600th cycle, it delivers a high capacity of 787.4 mA h g⁻¹, which still remains 87% capacity retention. Even at high current density of 5 A g⁻¹, the cycling capacity shows no significant fluctuations and can be still maintain a high capacity of 436.8 mA h g⁻¹ after 1600 cycles, corresponding to a CE of nearly 100%. It implies good cycling stability of N-C@Co₃O₄-CoO@GO. In contrast, the samples of Co₃O₄-CoO@GO and Co₃O₄-CoO show lower battery capacity and poor stability in terms of rate and cycle performance.

Such superior electrochemical performance of N-C@Co₃O₄-CoO@GO benefits from the following reasons. Firstly, the 3D structure of graphene and active material contributes to the rapid diffusion of Li ions and increases the contact area to promote effective penetration of the electrolyte. Next, the graphene can reduce volume expansion and

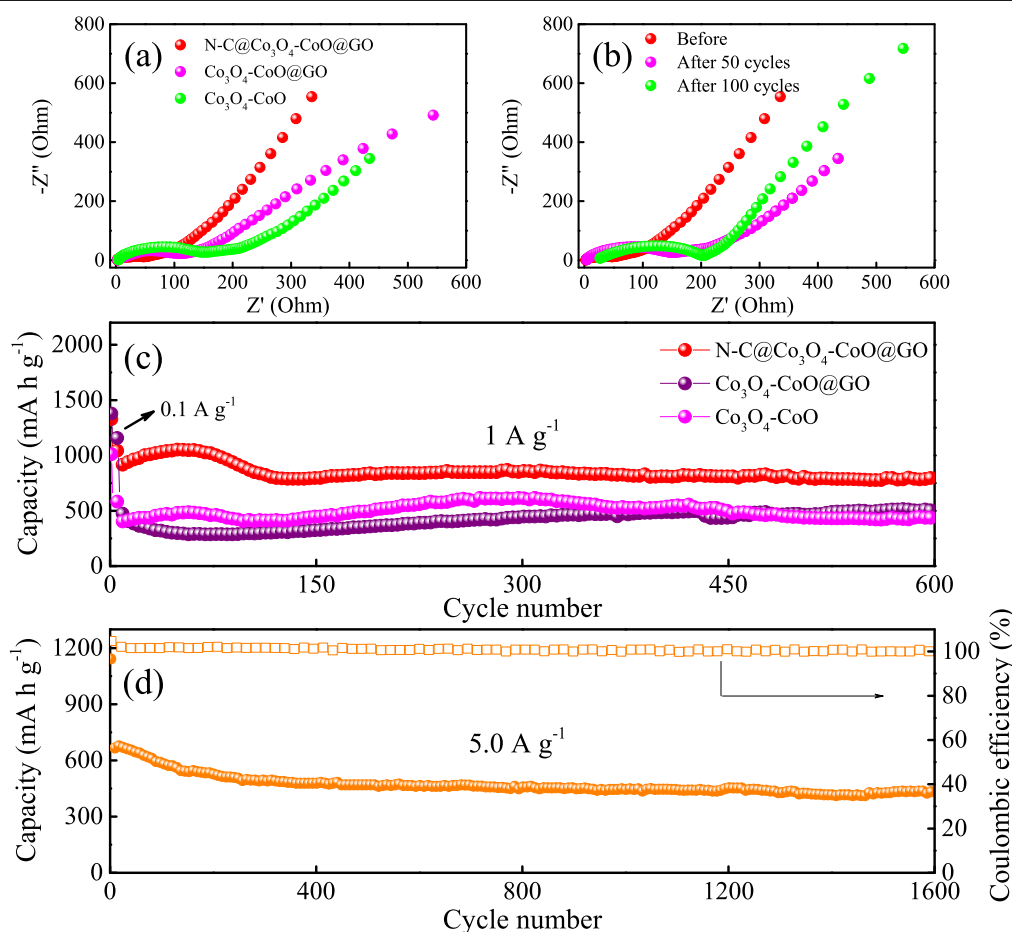


Figure 4. The electrochemical impedance spectra of (a) N-C@Co₃O₄-CoO@GO, Co₃O₄-CoO@GO and Co₃O₄-CoO electrodes. (b) The N-C@Co₃O₄-CoO@GO electrode before cycle, after 50 and 100 cycle over the frequency range from 100 kHz to 0.01 Hz. (c) Cycling performance comparison of N-C@Co₃O₄-CoO@GO, Co₃O₄-CoO@GO and Co₃O₄-CoO at the same current density of 1 A g⁻¹ for 600 cycles and (d) The N-C@Co₃O₄-CoO@GO electrode at a high current density of 5 A g⁻¹ for 1600 cycles after initial five cycles for activation at 0.1 A g⁻¹.

prevent particle agglomeration. Finally, the addition of amorphous N-doped carbon enhances electrical conductivity. Besides, we have also compared this work with those of previously reported Co₃O₄-based materials [37, 39, 41, 58, 60–64]. As shown in figure 3(e) and table S1, the capacity at different current density is generally higher and more stable than the previous materials. It can be seen that the materials obtained from the present work have excellent electrical properties. Additionally, in order to further understand the outstanding high capacity and stability of N-C@Co₃O₄-CoO@GO, the EIS measurements and the corresponding equivalent circuit diagram of all anode materials are displayed in figure 4(a) (all the samples are measured in the initial state) and figure S7, respectively. Figure 4(a) reveals the typical Nyquist curves of the electrodes and the curve of equivalent electrical circuit consists of the electrolyte resistance (R_s), a semicircle in the high frequency region related to the diffusion and migration resistance of lithium ions through the SEI film (R_f), a medium-frequency semicircle correspond to the charge transfer resistance (R_{ct}) and a sloping line in the low-frequency region attributed to the solid diffusion process of lithium ions (the Warburg impedance, Z_w) [56, 65]. In figure S7, the circuit fitted R_f and R_{ct} values of N-C@Co₃O₄-CoO@GO electrode are 6.89

and 26.4 Ω , respectively, while for the Co₃O₄-CoO@GO and Co₃O₄-CoO electrodes, the values of R_f and R_{ct} increase to 11.77/107 Ω and 18.09/108 Ω , respectively. It confirms prominent lithium ion diffusion ability and rapid charge transfer rate for the N-C@Co₃O₄-CoO@GO electrode, which benefit from a unique 3D structure composed of active materials, graphene oxide sheets and the introduction of conductive nitrogen carbon. Similarly, the above three frequency region characterizations also exhibit in the Nyquist curve of N-C@Co₃O₄-CoO@GO electrode tested before (the initial state) and after cycling (the fully charged states) at 1 A g⁻¹ (figure 4(b)). The semicircle size of the high-medium frequency region for N-C@Co₃O₄-CoO@GO electrodes before cycling is significantly smaller than that after 50 and 100 cycles. It suggests that the rapid diffusion of lithium ions and charge transfer benefit from SEI film gradually formed and sufficient contact of electrolyte with electrode. As the number of cycles increases, the decomposition of the electrolyte causes the charge transfer to be hindered. The slope of the low-frequency region after 100 cycle is larger than that after 50 cycles, implying increased internal active sites in materials during lithiation and delithiation process [66]. In addition, the intercept of the high-frequency region in the

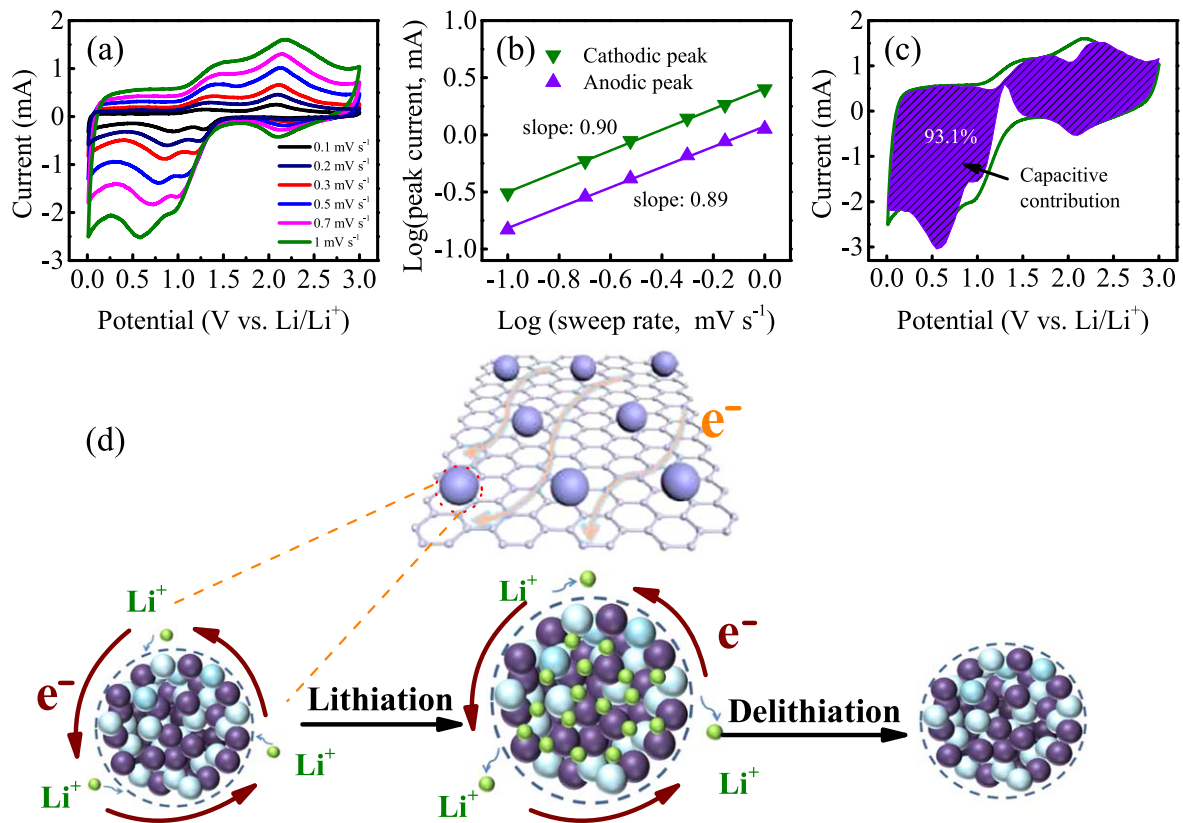


Figure 5. (a) The CV curves of the N-C@Co₃O₄-CoO@GO electrode at different scanning rates from 0.1 to 1 mV s⁻¹. (b) Determination of the b value using the relationship between logarithm peak current and logarithm scanning rates for N-C@Co₃O₄-CoO@GO electrode according to the voltammograms in (a). (c) The capacitive contribution to charge storage at a scanning rate of 1 mV s⁻¹. (d) Schematic of structural change of the N-C@Co₃O₄-CoO@GO electrode during the lithiation/delithiation process.

Z'-axis significantly increases after 100 cycles, indicating that the internal resistance of the electrolyte increases. It may be due to the partial shedding of small amount of active material caused by the volume expansion during the reaction of the battery and the partial decomposition of the electrolyte during the reaction.

To explore the redox kinetic electrochemical behaviors of the electrodes, the CV tests were conducted at the various scanning rates ranging from 0.1 to 1 mV s⁻¹ as shown in figure 5(a) and figures S8(a), (b). Compared with Co₃O₄-CoO@GO and Co₃O₄-CoO, the obvious and well-separated redox peak shape of N-C@Co₃O₄-CoO@GO has almost no change and the peak voltage has only tiny shift with the increase of scanning rate, suggesting the rapid insertion and extraction of lithium with smaller polarization effects. Figure 5(d) schematically illustrates the structural transformation of the N-C@Co₃O₄-CoO@GO electrode during the lithiation/delithiation process. The outstanding flexibility of graphene sheets alleviates the volume change of N-C@Co₃O₄-CoO@GO composite and prevents agglomeration of Co₃O₄-CoO nanoparticles. Additionally, it offers more conductive paths for rapid charge transfer. Besides, the entire area of the CV curve represents the total amount of lithium storage during the electrochemical reaction. As we know, the lithium storage mechanism includes the contribution of lithium ion diffusion during the lithiation/delithiation process and the capacitive contribution during surface charge

transfer process (also referred to as pseudocapacitance) [67, 68]. It could be characterized by the relationship between peak current (*i*) and scanning rate (*ν*), according to the following equations [69]:

$$i = a\nu^b, \quad (3)$$

$$\log i = \log a + b \log \nu, \quad (4)$$

in which, *a* and *b* are adjustable constants. Generally speaking, the *b* value reflects the kinetics process of the electrochemical reaction. According to previous reports, if *b* = 0.5, the electrochemical reactions are attributed to the diffusion process; if *b* = 1, the electrochemical reactions are mainly due to the capacitive process; if 0.5 < *b* < 1, two mechanisms coexist for lithium ion storage [70, 71]. As shown in figure 5(b), the values of *b* for the cathodic peak and anodic peak of N-C@Co₃O₄-CoO@GO obtained from the slope of the log (*i*) versus log (*ν*) plot are 0.90 and 0.89, respectively. It implies that the N-C@Co₃O₄-CoO@GO electrode is dominated by the surface induced capacitance process. Meanwhile, the higher *b* value of N-C@Co₃O₄-CoO@GO electrode than that of Co₃O₄-CoO@GO and Co₃O₄-CoO (figures S8(c), (d)) reveals more capacitance contribution. It confirms that the addition of GO and N-doped carbon are beneficial to capacitive-controlled lithium storage, resulting in enhanced rate specific capacity and cycle stability. Furthermore, the capacitance contribution can be calculated quantitatively from the following equations [72]:

$$i(V) = k_1\nu + k_2\nu^{1/2}, \quad (5)$$

$$i(V)/\nu^{1/2} = k_1\nu^{1/2} + k_2, \quad (6)$$

where $k_1\nu$ and $k_2\nu^{1/2}$ correspond to the capacitance contributions from the surface-capacitive effects and diffusion-controlled process, respectively. k_1 and k_2 can be calculated by the peak current at a certain potential. By determining the values of k_1 and k_2 , we can calculate the ratio of the current at each characteristic voltage. Thus, we are able to obtain the specific contribution of the surface-capacitive and diffusion-controlled reaction process on the total capacity in the electrode. At the scanning rate of 1 mV s^{-1} (figure 5(c)), the capacitance contribution reaches up to 93.1% of the total storage. This pseudocapacitive effect accelerates the transfer of the surface charge, giving rise to the high rate capacity and superior cycle performance.

4. Conclusion

In summary, a novel three dimension porous N-C@Co₃O₄-CoO@GO conductive structure, which comprises thin-layered graphene sheets, a Co₃O₄-CoO composite nanoparticle and N-doped carbon, was synthesized by a simple one-step hydrothermal method. The resulting composite exhibits great potential for LIBs in terms of high reversible capacity, long cycling stability and maintaining good capacity under high current density. Specifically, the hybrid electrode of N-C@Co₃O₄-CoO@GO reveals stable and high capacity at different current densities and could reach a reversible capacity of $1273.1 \text{ mA h g}^{-1}$ after 30 cycles at a current density of 0.1 A g^{-1} . In addition, the N-C@Co₃O₄-CoO@GO electrode obtains a reversible capacity of $787.4 \text{ mA h g}^{-1}$ (a capacity retention of 87%) after 600 cycles at 1 A g^{-1} . Even at a ultrahigh current density of 5 A g^{-1} , it is still able to achieve relatively high reversible capacity of $436.8 \text{ mA h g}^{-1}$ after the ultra-long 1600 cycles. The superior electrical performance benefits from this unique structure and it is expected that this design would provide a potential strategy for other similar transition metal oxide anode-based materials.

Acknowledgments

This work was financially supported by the National Key R&D Program of China (Grant Nos. 2017YFA0303403 and 2018YFB0406500), the National Natural Science Foundation of China (Grant Nos. 61674057 and 91833303), the Projects of Science and Technology Commission of Shanghai Municipality (Grant Nos. 18JC1412400, 18YF1407200, and 18YF1407000), and the Program for Professor of Special Appointment (Eastern Scholar) at Shanghai Institutions of Higher Learning.

ORCID iDs

Yawei Li  <https://orcid.org/0000-0001-8776-5687>
Zhigao Hu  <https://orcid.org/0000-0003-0575-2191>

References

- [1] Sun Y Q, Wu Q and Shi G Q 2011 *Energy Environ. Sci.* **4** 1113–32
- [2] Etacheri V, Marom R, Elazari R, Salitra G and Aurbach D 2011 *Energy Environ. Sci.* **4** 3243–62
- [3] Goodenough J B and Park K S 2013 *J. Am. Chem. Soc.* **135** 1167–76
- [4] Chen Y M, Yu L and Lou X W 2016 *Angew. Chem.* **128** 6094–7
- [5] Wang L, Zhang K, Hu Z, Duan W, Cheng F and Chen J 2013 *Nano Res.* **7** 199–208
- [6] Huang X L, Wang R Z, Xu D, Wang Z L, Wang H G, Xu J J, Wu Z, Liu Q C, Zhang Y and Zhang X B 2013 *Adv. Funct. Mater.* **23** 4345–53
- [7] Guo W, Sun W, Lv L-P, Kong S and Wang Y 2017 *ACS Nano* **11** 4198–205
- [8] Yuan S, Wang S, Li L, Zhu Y H, Zhang X B and Yan J M 2016 *ACS Appl. Mater. Interfaces* **8** 9178–84
- [9] Xia G, Zhang L, Fang F, Sun D, Guo Z, Liu H and Yu X 2016 *Adv. Funct. Mater.* **26** 6188–96
- [10] Ji L W, Lin Z, Alcoutlabi M and Zhang X W 2011 *Energy Environ. Sci.* **4** 2682–99
- [11] Karunakaran G, Kundu M, Kumari S, Kolesnikov E, Gorshenkov M V, Maduraiveeran G, Sasidharan M and Kuznetsov D 2018 *J. Alloys Compd.* **763** 94–101
- [12] Kundu M, Karunakaran G, Kumari S, Minh N V, Kolesnikov E, Gorshenkov M V and Kuznetsov D 2017 *J. Alloys Compd.* **725** 665–72
- [13] Xue H J, Na Z L, Wu Y Q, Wang X X, Li Q, Liang F, Yin D M, Wang L M and Ming J 2018 *J. Mater. Chem. A* **6** 12466–74
- [14] Han Y Z, Li J, Zhang T Y, Qi P F, Li S W, Gao X, Zhou J W, Feng X and Wang B 2018 *Chem. Eur. J.* **24** 1651–6
- [15] Lou X W, Deng D, Lee J Y, Feng J and Archer L A 2015 *Adv. Mater.* **7** 2882–90
- [16] Wang H, Mao N, Shi J, Wang Q, Yu W and Wang X 2015 *ACS Appl. Mater. Interfaces.* **7** 2882–90
- [17] Xiao X, Liu X, Zhao H, Chen D, Liu F, Xiang J, Hu Z and Li Y 2012 *Adv. Mater.* **24** 5762–6
- [18] Wang B, Lu X Y and Tang Y Y 2015 *J. Mater. Chem. A* **3** 9689–99
- [19] Chen S Q and Wang Y 2010 *J. Mater. Chem.* **20** 9735–9
- [20] Kundu M, Singh G and Svensson A M 2019 *New J. Chem.* **43** 1257–66
- [21] Kim Y et al 2014 *J. Mater. Chem.* **8** 6701–12
- [22] Peng L, Feng Y, Bai Y, Qiu H-J and Wang Y 2015 *J. Mater. Chem. A* **3** 8825–31
- [23] Li Y G, Tan B and Wu Y Y 2008 *Nano Lett.* **8** 265–70
- [24] Nam K T, Kim D W, Yoo P J, Chiang C Y, Meethong N, Hammond P T, Chiang Y M and Belcher A M 2006 *Science* **312** 885–8
- [25] Karunakaran G, Kundu M, Maduraiveeran G, Kolesnikova E, Gorshenkov M V, Kannan Balasingam S, Kumari S, Sasidharan M and Kuznetsov D 2018 *Microporous Mesoporous Mater.* **272** 1–7
- [26] Sun Y, Huang F Z, Li S K, Shen Y H and Xie A J 2017 *Nano Res.* **10** 3457–67
- [27] Huang J, Ma Y T, Xie Q S, Zheng H F, Yang J R, Wang L S and Peng D L 2018 *Small* **14** 1703513

- [28] Zhang L H, Wei T, Jiang Z M, Liu C Q, Jiang H, Chang J, Sheng L Z, Zhou Q H, Yuan L B and Fan Z J 2018 *Nano Energy* **48** 238–47
- [29] Zhang H, Wang Y, Zhao W, Zou M, Chen Y, Yang L, Xu L, Wu H and Cao A 2017 *ACS Appl. Mater. Interfaces* **9** 37813–22
- [30] Luo B and Zhi L J 2015 *Energy Environ. Sci.* **8** 456–77
- [31] Jeong J M, Choi B G, Lee S C, Lee K G, Chang S J, Han Y K, Lee Y B, Lee H U, Kwon S and Lee G 2013 *Adv. Mater.* **25** 6250–5
- [32] Wang Z H, Qie L, Yuan L X, Zhang W X, Hu X L and Huang Y H 2013 *Carbon* **55** 328
- [33] Han X, Chen W M, Han X, Tan Y Z and Sun D 2016 *J. Mater. Chem. A* **4** 13040–5
- [34] Cao F et al 2016 *J. Am. Chem. Soc.* **138** 6924–7
- [35] Sun X L et al 2016 *J. Mater. Chem. A* **4** 10166–73
- [36] Hou Q D, Man Q R, Liu P F, Jin R C, Cui Y M, Li G H and Gao S M 2019 *Electrochim. Acta* **296** 438–49
- [37] Mujtaba J, Sun H Y, Zhao Y, Xiang G L, Xu S M and Zhu J 2017 *J. Power Sources* **363** 110–6
- [38] Park G D, Lee J-K and Kang Y C 2017 *J. Mater. Chem. A* **5** 25319–27
- [39] Fang G Z, Zhou J, Cai Y S, Liu S N, Tan X P, Pan A Q and Liang S Q 2017 *J. Mater. Chem. A* **5** 13983–93
- [40] Hummers W S and Offeman R E 1958 *J. Am. Chem. Soc.* **80** 1339–1339
- [41] Zhu S, Li J J, Deng X Y, He C N, Liu E Z, He F, Shi C S and Zhao N Q 2017 *Adv. Funct. Mater.* **27** 1605017
- [42] Wang S H, Chen M Q, Xie Y Y, Fan Y N, Wang D W, Jiang J J, Li Y G, Grutzmacher H J and Su C Y 2016 *Small* **17** 2365–75
- [43] Dou Y H, Xu J T, Ruan B Y, Liu Q N, Pan Y D, Sun Z Q and Dou S X 2016 *Adv. Energy Mater.* **6** 1501835
- [44] He J R, Chen Y F, Li P J, Fu F, Wang Z G and Zhang W L 2015 *J. Mater. Chem. A* **3** 18605–10
- [45] Kang W P, Zhang Y, Fan L L, Zhang L L, Dai F N, Wang R M and Sun D F 2017 *ACS Appl. Mater. Interfaces* **9** 10602–9
- [46] Liu X et al 2015 *Adv. Funct. Mater.* **25** 5799–808
- [47] Zhou S S, Ye Z C, Hu S Z, Hao C, Wang X H, Huang C X and Wu F S 2018 *Nanoscale* **10** 15771–81
- [48] Peng C, Chen B, Qin Y, Yang S, Li C, Zuo Y, Liu S and Yang J 2016 *ACS Nano* **6** 1074
- [49] Xu M W, Wang F, Zhang Y, Yang S, Zhao M S and Song X P 2013 *Nanoscale* **5** 8067–72
- [50] Abouali S, Garakani M A, Zhang B, Luo H, Xu Z L, Huang J Q, Huang J and Kim J K 2014 *J. Mater. Chem. A* **2** 16939–44
- [51] Xie K, Wu P, Zhou Y, Ye Y, Wang H, Tang Y, Zhou Y and Lu T 2014 *ACS Appl. Mater. Interfaces* **6** 10602
- [52] Wu Z S, Ren W, Wen L, Gao L, Zhao J, Chen Z, Zhou G, Li F and Cheng H M 2010 *ACS Nano* **4** 3187–94
- [53] Yan C S, Chen G, Zhou X, Sun J X and Lv C D 2016 *Adv. Funct. Mater.* **26** 1428
- [54] Wei W, Yang S, Zhou H, Lieberwirth I, Feng X and Mullen K 2013 *Adv. Mater.* **25** 2909–14
- [55] Huang G Y, Xu S M, Lu S S, Li L Y and Sun H Y 2014 *ACS Appl. Mater. Interfaces* **6** 7236–43
- [56] Xu M W, Wang F, Zhang Y, Yang S, Zhao M S and Song X P 2013 *Nanoscale* **5** 8067–72
- [57] Sun H, Xin G, Hu T, Yu M, Shao D, Sun X and Lian J 2014 *Nat. Commun.* **5** 4526
- [58] Huang G, Zhang F, Du X, Qin Y, Yin D and Wang L 2015 *ACS Nano* **9** 1592–9
- [59] Du H R, Yuan C, Huang K F, Wang W H, Zhang K and Geng B Y 2017 *J. Mater. Chem. A* **5** 5342–50
- [60] Lu Y, Yu L, Wu M H, Wang Y and Lou X W 2018 *Adv. Mater.* **30** 1702875
- [61] Chen Y J, Wang Y S, Wang Z P, Zou M C, Zhang H, Zhao W Q, Yousaf M H, Yang L S, Cao A Y and Ray P S H 2018 *Adv. Energy Mater.* **8** 1702981
- [62] Jing M J, Zhou M J, Li G Y, Chen Z G, Xu W Y, Chen X B and Hou Z H 2017 *ACS Appl. Mater. Interfaces* **9** 9662–8
- [63] Sui Z Y, Zhang P Y, Xu M Y, Liu Y W, Wei Z X and Han B H 2017 *ACS Appl. Mater. Interfaces* **9** 43171–8
- [64] Wang Y Z, Kong M G, Liu Z W, Lina C C and Zeng Y 2017 *J. Mater. Chem. A* **5** 24269–74
- [65] Lee W W and Lee J M 2014 *J. Mater. Chem. A* **2** 1589
- [66] Cao W Q, Wang W Z, Shi H L, Wang J, Cao M S, Liang Y J and Zhu M 2018 *Nano Res.* **11** 1437–46
- [67] Liu Y W et al 2017 *ACS Nano* **11** 8519–26
- [68] Augustyn V, Simon P and Dunn B 2014 *Energy Environ. Sci.* **7** 1597–614
- [69] Wang C, Fang Y, Xu Y, Liang L, Zhou M, Zhao H and Lei Y 2016 *Adv. Funct. Mater.* **26** 1777–86
- [70] Lou P, Cui Z, Jia Z, Sun J, Tan Y and Guo X 2017 *ACS Nano* **11** 3705–15
- [71] Song Y, Chen Z, Li Y, Wang Q, Fang F, Zhou Y N, Hu L and Sun D 2017 *J. Mater. Chem. A* **5** 9022–31
- [72] Brezesinski T, Wang J, Tolbert S H and Dunn B 2010 *Nat. Mater.* **9** 146–51